JOURNAL OF MATERIALS SCIENCE 19 (1984) 533–544

High resolution electron microscopy in association with interactive computing

J. C. JONES*
Department of Metallurgy and Science of Materials, University of Oxford, Oxford, UK

Although facilities for high resolution electron microscopy (HREM) are available, interpretation of micrographs at high magnifications is far from unambiguous. The interpretation of the micrographs using a computed structure analysis program is therefore necessary. The paper presents the theory behind HREM, together with a computer method for image interpretation. Special reference is made to the JEOL JEM 200CX transmission electron microscope used in the study of sodium beta-alumina.

1. Introduction to high resolution electron microscopy

The theory and practice of electron microscopy has graduated into very high resolution work, involving the study of the structure of matter by imaging the individual atoms of which it is composed. The resolution necessary to achieve this is obtainable, in principle, because beams of electrons with wavelengths less than 0.1 nm are relatively easily produced. However, only recently have electron microscopes been produced with aberrations sufficiently low that atomic resolution is a practical possibility.

The minimum resolvable distance in a microscope is of the order of the wavelength of the illumination used. This is the fundamental limit set by diffraction and applies to both coherent and incoherent illumination. Therefore, for resolving crystal lattices or defects on an atomic scale, a wavelength of $\lambda < 0.1$ nm is needed, which suggests the use of fast electrons, X-rays or neutrons.

Electrons are charged particles, and are therefore scattered by the nucleus and orbital electrons of an atom. X-rays are weakly scattered essentially only by atomic electrons, and neutrons are scattered only by atomic neuclei or by atoms possessing magnetic moments. The fact that electrons are charged means that they may be focused by electromagnetic lenses, and hence diffraction patterns and highly magnified images may be produced. X-rays and neutrons cannot be focused, so magnification of the image is not possible. In the case of fast electrons, the radius of the Ewald sphere is very large in comparison with a typical reciprocal lattice vector ($\mathbf{k} = \lambda^{-1} \sim 400$ nm^{-1}), so electron diffraction patterns correspond roughly to a plane section of the reciprocal lattice taken perpendicular to the direction of the incident beam. This may be compared with the cases for X-rays and neutrons where it is difficult to orient the crystal to obtain even one diffracted beam (for constant λ). Fast electrons are not limited by this difficulty, and are the only possible radiation for imaging fine structure.

2. The principles of transmission electron microscopy

HREM has been carried out using the Jeol 200CX transmission electron microscope (TEM). The gun contains a filament of LaB_6, and the generated electrons are accelerated through 200 kV. The two condenser lenses focus the electrons onto the object lying in the centre of the objective lens, the quality of which determines the resolution in the image. Any astigmatism in the objective lens may be corrected by adjusting the stigmators, whilst the image is slightly out of focus, until a uniform Fresnel fringe (either dark or light) is obtained on a feature within the image. This may be a hole in the carbon film supporting the specimen. Also, the fine structure within the carbon

*Present address: Scientific Services Department, Central Electricity Generating Board, Gravesend, Kent, UK.

0022–2461/84 $03.00 + .12 © *1984 Chapman and Hall Ltd.*

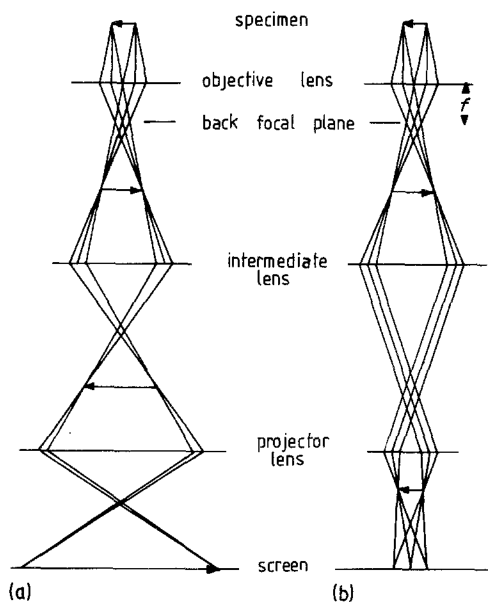

Figure 1 Ray diagrams for (a) imaging mode and (b) diffraction mode.

film must be observed at high magnification to ensure there is no preferential direction within the grainy structure. Minimum contrast within the carbon film ensures that the specimen is in focus. By going out of focus, the contrast increases, but is of opposite sign for over- and under-focus.

A range of magnification, up to about 750 000 times, may be provided by the subsequent lens combinations. Diffraction patterns are obtained by increasing the focal length of the intermediate lens until the back focal plane of the objective lens is conjugate to the final viewing screen. Both imaging and diffraction modes are shown in the ray diagrams of Fig. 1. Selected area diffraction enables diffraction patterns to be taken from small areas of the specimen, so that a correlation between features observed on the micrographs and the crystallography of the specimen can be made. Spherical aberration is the most important lens defect: it has the effect of retarding the phases of beams off the optic axis. For the Jeol 200CX, the spherical aberration coefficient, c_s, is 1.2 mm.

3. Lattice imaging

For lattice imaging, crystals must be investigated in specific orientations. Interference fringes with the periodicity of the lattice planes are produced when several diffracted beams go through the objective aperture. A sufficiently thin crystal, over a hole in the carbon film, is centred in the selected area aperture, and is then tilted in two perpendicular directions whilst viewing the diffraction pattern until the required orientation is obtained with a given zone axis $(u\,v\,w)$ parallel to the incident beam direction. The two-dimensional diffraction pattern obtained contains beams $h\,k\,l$, where $hu + kv + lw = 0$, and the two-dimensional lattice image contains information about the crystal in the plane perpendicular to the zone axis. An objective aperture is normally used so that all beams within a certain (reciprocal) distance of the origin contribute to the image. The above method of lattice imaging is known as zone axis orientation imaging.

The treatment of image interpretation is greatly simplified if the weak phase object approximation is made. Electrons interact with very thin objects as if they are pure phase objects, and so a perfect, focused image would be expected to show no contrast. In practice, however, there is always some contrast due to the modification of amplitude and phase of constituent waves by the objective lens. Image contrast does not correspond precisely to the structure of the specimen, so image interpretation is critical.

There are two resolution criteria important for the weak phase object. The image of the object may be easily interpreted down to the "point resolution", defined as the spacing corresponding to the first zero of $\sin\chi$ (defined later) at the Scherzer defocus. This gives the best representation of the projected potential with an objective aperture chose to cut off the $\sin\chi$ function before it starts oscillating rapidly at higher scattering angles. For any electron microscope, the point resolution is $0.66\,c_s^{1/4}\lambda^{3/4}$. Specifically for the JEOL 200CX, this is 0.245 nm. Object detail beyond the point resolution may be obtained by image processing or comparison of a through-focal series, but not beyond the second resolution criterion, known as the "information resolution limit". This is determined by the chromatic damping envelope of the contrast transfer function, and is due to the energy spread of electrons from the source, and also high tension and lens current instabilities. For the Jeol 200CX, the information resolution limit is at least 0.17 nm.

4. The theory of image formation

The basic concepts of image formation in an electron microscope may be conveniently described

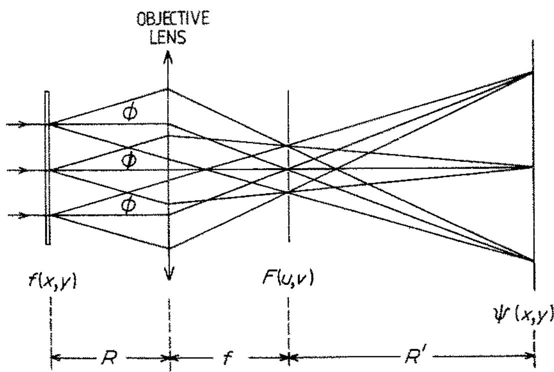

Figure 2 The Abbé theory of image formation.

by the Abbé principle of imaging, a ray diagram for which is shown in Fig. 2. A more detailed mathematical treatment of the following theory may be found in [1–4].

When parallel, coherent radiation is incident on an object of transmission function $f(x, y)$, the imaging process may be described in terms of two Fourier transforms. The incident beam can be approximated to a plane wave of unit amplitude, so the wave leaving the object also has amplitude $f(x, y)$. Parallel, scattered beams from the object are brought to a focus by an objective lens, and interfere on the back focal plane to give a Fraunhofer diffraction pattern. This amplitude distribution is described by the Fourier transforms of the transmission function of the object, given by $F(u, v)$. In this case, $u = \sin \phi_x/\lambda$, and if ϕ, the scattering angle, is small, then $u = x/f\lambda$ and $v = y/f\lambda$, where f is the focal length of the objective lens as shown diagrammatically in Fig. 2. The electrons propagate from the back focal plane to form an interference pattern in the image plane, so the amplitude distribution in the image, $\psi(x, y)$, is given by the Fourier transform of that in the back focal plane:

$$\psi(x, y) = f\left(\frac{-Rx}{R'}, \frac{-Ry}{R'}\right)$$

where $-R/R'$ is the magnification. Hence the final image is identical to the transmission function of the object, except that it is inverted and magnified. For convenience, it is usual to put

$$\psi(x, y) = f(x, y). \qquad (1)$$

The effects of aperture limitations and aberrations of the lens system in reproducing the object transmission function in the image plane may be considered in terms of modifications of the amplitude and phase of the distribution on the back focal plane. These changes affect the intensity variations in the image, and may be described as the result of multiplication by an optical transfer function. Consequently, there is a loss of resolution since the transfer function "spreads out" the image of a point in the object.

The effect of the insertion of an objective lens aperture is represented by multiplying the amplitude distribution in the back focal plane of the objective, $F(u, v)$, by an aperture function, $A(u, v)$, which is unity within the aperture and zero outside it. The defocus of the lens by an amount, Δ, and the effect of spherical aberration, also introduce changes of phase in the amplitude. These corrections give an expression for the amplitude of

$$F'(u, v) = F(u, v) \times A(u, v) \times \exp[i\chi(u, v)] \qquad (2)$$

where $\chi(u, v)$ is the phase factor incorporating the two phase effects mentioned above, and is given by:

$$\chi(u, v) = \pi\Delta\lambda(u^2 + v^2) + \frac{\pi}{2}c_s\lambda^3(u^2 + v^2)^2. \qquad (3)$$

In general, therefore, the wave function in the back focal plane is multiplied by a contrast transfer function, $T(u, v)$, which modifies its amplitude and phase, where:

$$T(u, v) = A(u, v) \exp[i\chi(u, v)].$$

The transmission function of the object, if treated as a phase object, is given by:

$$f(x, y) = \exp[-i\sigma\phi(x, y)]$$

where σ is the interaction constant, $\pi/\lambda E$, for an accelerating voltage E, and $\phi(x, y)$ is the projected potential of the crystal in the beam direction. For sufficiently thin specimens involving light atoms, where it may be assumed that $\sigma\phi(x, y) \ll 1$, then, to a reasonable approximation,

$$f(x, y) = 1 - i\sigma\phi(x, y).$$

This is the weak phase object approximation. Earlier, it was stated that a pure phase object, perfectly focused in an ideal microscope, reveals no contrast. If a plane incident wave falls on this object, the transmitted intensity would be

$$I(x, y) = |f(x, y)|^2 = 1.$$

Similarly, an ideal lens would reproduce $f(x, y)$

exactly, so the intensity distribution in the image would be:

$$I(x,y) = |\psi(x,y)|^2 = 1.$$

For an imperfect lens, the amplitude in the back focal plane, from Equation 2, is:

$$\Psi(u,v) = [\delta(u,v) - i\sigma\Phi(u,v)] \times T(u,v),$$

where $\Phi(u,v)$ is the Fourier transforms of $\phi(x,y)$ and represents the scattered radiation. The delta function represents the directly transmitted incident beam.

The loss of resolution in the image, due to spherical aberration and defocus, may be described in terms of a spread function in the image plane, $s(x,y)$ which is the Fourier transform of the contrast function. Hence, the image amplitude in Equation 1 is modified to:

$$\psi(x,y) = |1 - i\sigma\phi(x,y)| \star s(x,y) \qquad (4)$$

where $\star$ denotes convolution. Only the imaginary part of the spread function is important for a weak phase object (the real part contributes to second order terms). Hence, the contrast transfer function $\exp|i\chi(u,v)|$, reduces to $\sin\chi(u,v)$, the variation of which with spatial frequency gives the well-known oscillatory representation of the contrast transfer function.

Phase contrast is converted to amplitude contrast through defocusing by an amount which introduces an additional phase change of $\pm\pi/2$ to scattered beams. For a small range of defocus values about an optimum defocus, there will therefore be an optimum image if an objective aperture is used such that only diffracted beams for which $\sin\chi$ is unity are allowed to contribute to the image. The intensity then varies linearly with the projected potential, i.e. (from Equation 4):

$$I(x,y) = 1 \pm 2\sigma\phi(x,y)$$

and hence the image is easily interpreted provided a weak phase object is used.

The phase factor $\chi(u,v)$ is given by Equation 3. Electron microscope systems have cylindrical symmetry, and so the spatial frequency may be used as a single radial coordinate, giving:

$$\chi(u) = \pi\Delta\lambda u^2 + \frac{\pi}{2}c_s\lambda^3u^4. \qquad (5)$$

The contrast transfer function (CTF) is most easily represented as a plot of $\sin\chi(u)$ against the spatial frequency, u, for various values of defocus. Examples of these are given in Fig. 3. The optimum defocus producing image contrast from a weak phase object is when $\sin\chi$ is close to ± 1 for the largest range of spatial frequency. Scherzer originally suggested a defocus value for which $\chi(u) \sim -\pi/2$ for a range of frequencies. This yields:

$$\Delta = -(c_s\lambda)^{1/2}.$$

A smaller point resolution may be achieved by choosing a value for $\chi(u)$ of $\sim -2\pi/3$ for a range of frequencies. An expression for the optimum defocus is found by putting $d\chi/du = 0$, and substituting for u^2 from this expression in Equation 5, we obtain:

$$\Delta_{opt} = -(\tfrac{4}{3}c_s\lambda)^{1/2}$$

which corresponds to an optimum aperture size of

$$u_{max} = 1.52 \times c_s^{-1/4}\lambda^{-3/4}$$

and the least resolvable distance in the image is therefore $0.66\,c_s^{1/4}\lambda^{3/4}$. This suggests that the resolution may be improved by decreasing c_s or by using radiation of smaller wavelength, the latter being more effective. However, this requires a higher accelerating voltage, which tends to cause the c_s value to deteriorate.

Image interpretation beyond the point resolution is not straightforward due to the oscillatory nature of $\sin\chi$. However, as shown in Fig. 3, the CTF may develop small plateaux or kinks at certain defocus values. Here, a range of spatial frequencies may be transmitted where the effects of beam divergence damping are negligible and the information resolution limit is set by the chromatic damping term. For the parameters associated with the Jeol 200CX, the first few of these defocus values are -65 nm, -100 nm and -125 nm. Images may be produced beyond the point resolution of the microscope by using these "pass-bands", and also an objective aperture radius which corresponds to the value of the spatial frequency where the $\sin\chi$ function first intersects the u-axis after the plateau or kink has occurred.

5. Interactive computing

The only sure interpretation of lattice images is by comparison of experimental micrographs with computed images from n-beam dynamical calculations. The theory behind these computations is given in [5–10].

High resolution electron microscopy requires thin specimens for examination, and for crystals with large unit cells, such as sodium beta-alumina,

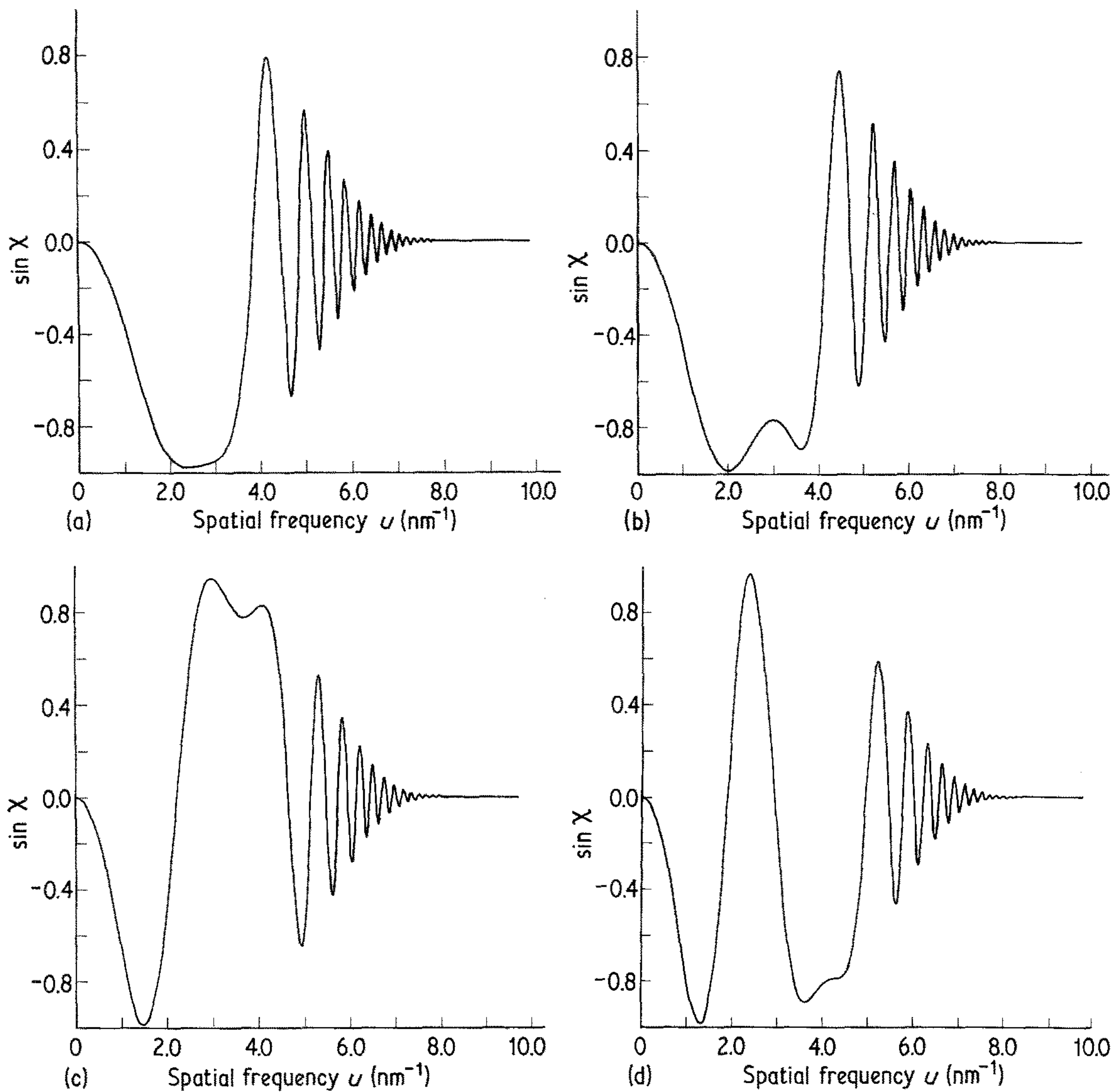

Figure 3 Contrast Transfer Function. (a) Scherzer defocus, —55 nm; (b) Optimum defocus, —65 nm; (c) Pass-band defocus, —100 nm; (d) Pass-band defocus, —125 nm.

many diffracted beams may be excited. The calculation of electron microscope images presents an ideal case for interactive computing, and involves the input of a crystal model from which is calculated an electron image. The multi-slice theory of Cowley and Moodie [11], as developed by Goodman and Moodie [12] is most useful for this. The material is treated as a series of planes, each one containing the projected potential from the above slice. These slices must be sufficiently thin so that errors introduced by having to take finite slices are minimized. For this reason, it is convenient to use a slice thickness corresponding to a fraction (or a multiple) of the plane separation in the z-direction (the electron beam direction).

The system used comprises five programs, controlled by the executive program EMIMAG [13]. The first program, PLOT, requires basic crystal structure parameters to plot a structure down any zone. These parameters are used in the second program FCOEFF to generate Fourier coefficients, which represent structure factors, and are used in the generation of the slice potentials in the multi-slice calculation, MULSLI. This program displays the single slice projected potential for the accelerating potential specified, and calculates the beam intensities used in the display of the simulated electron microscope image in the last program, IMAGE. There is also an option for the display of the electron diffraction pattern

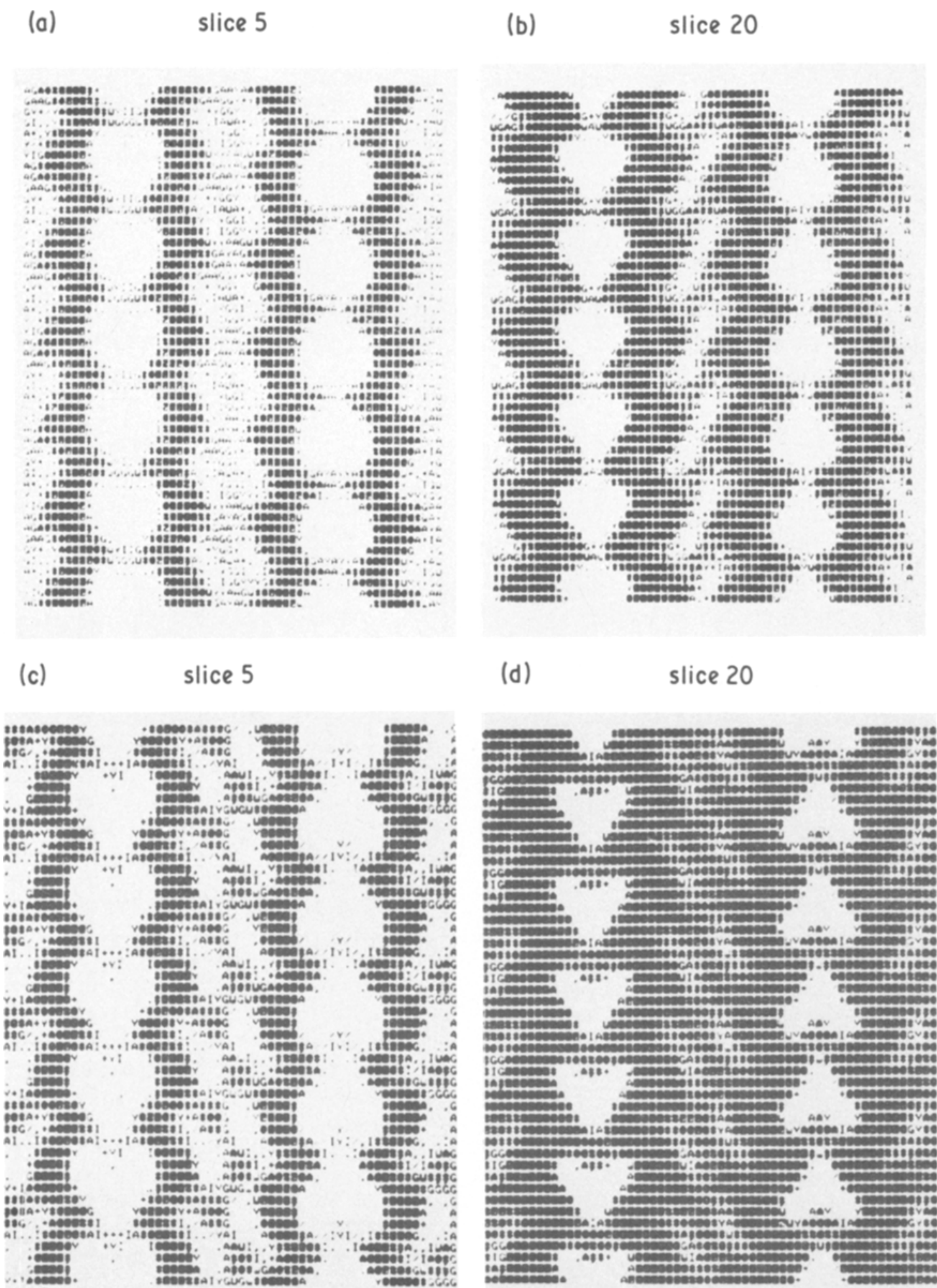

Figure 4 Computed images of sodium beta-alumina along $\langle 11\bar{2}0\rangle$ $R = 2.9\,\mathrm{nm}^{-1}$ at defocus values (a and b) −55 nm, (c and d) −65 nm, (e and f) −100 nm, (g and h) −125 nm. $R = 4.7\,\mathrm{nm}^{-1}$ at a defocus value of (i and j) −100 nm, and $R = 5.0\,\mathrm{nm}^{-1}$ at (k and l) −125 nm.

(e) slice 5

(f) slice 20

(g) slice 5

(h) slice 20

Figure 4 Continued.

(i) slice

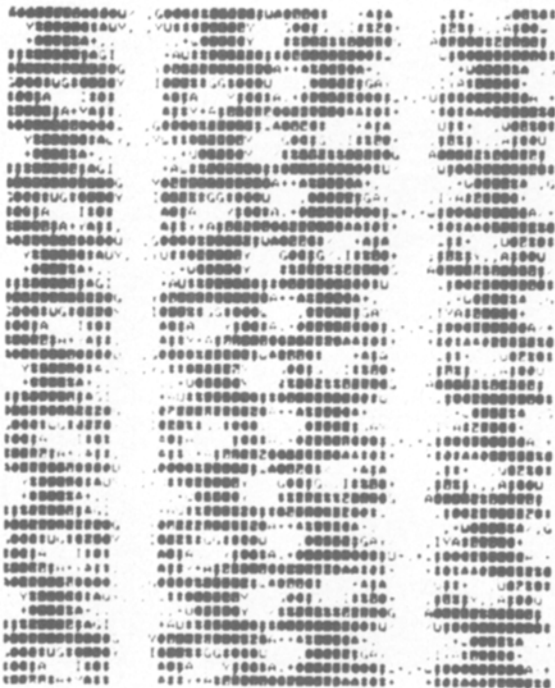

(j) slice 20

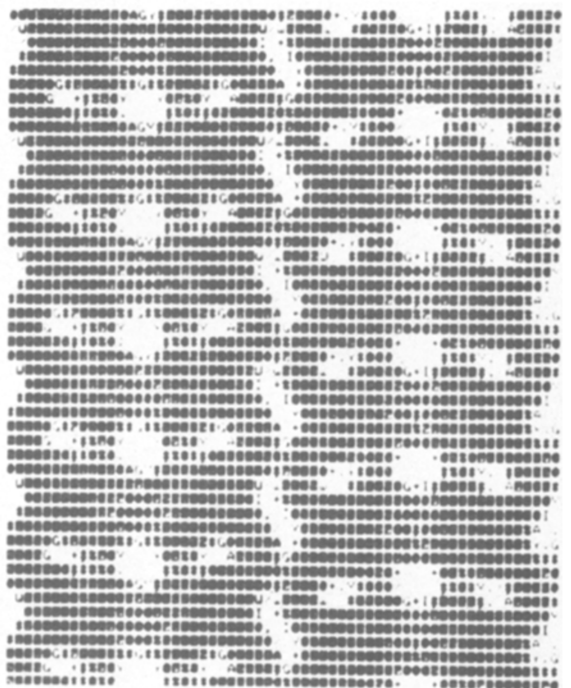

(k) slice 5

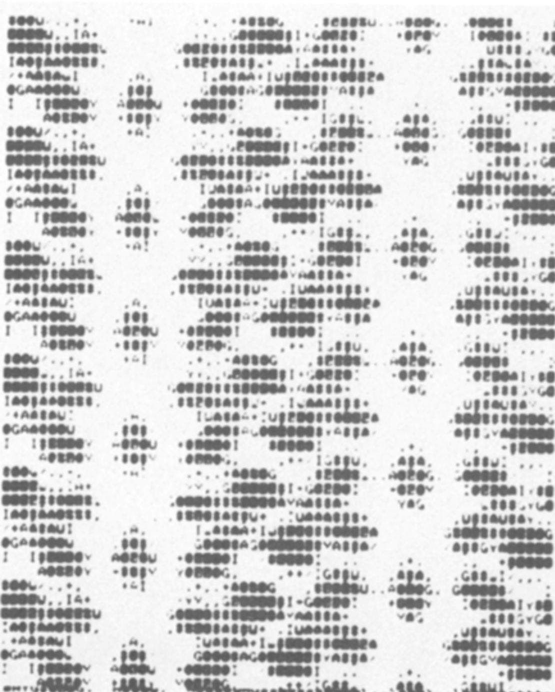

(l) slice 20

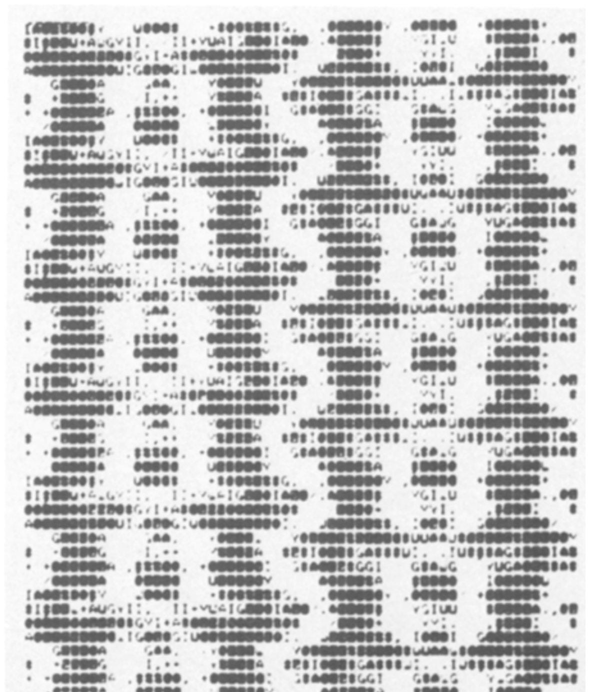

Figure 4 Continued.

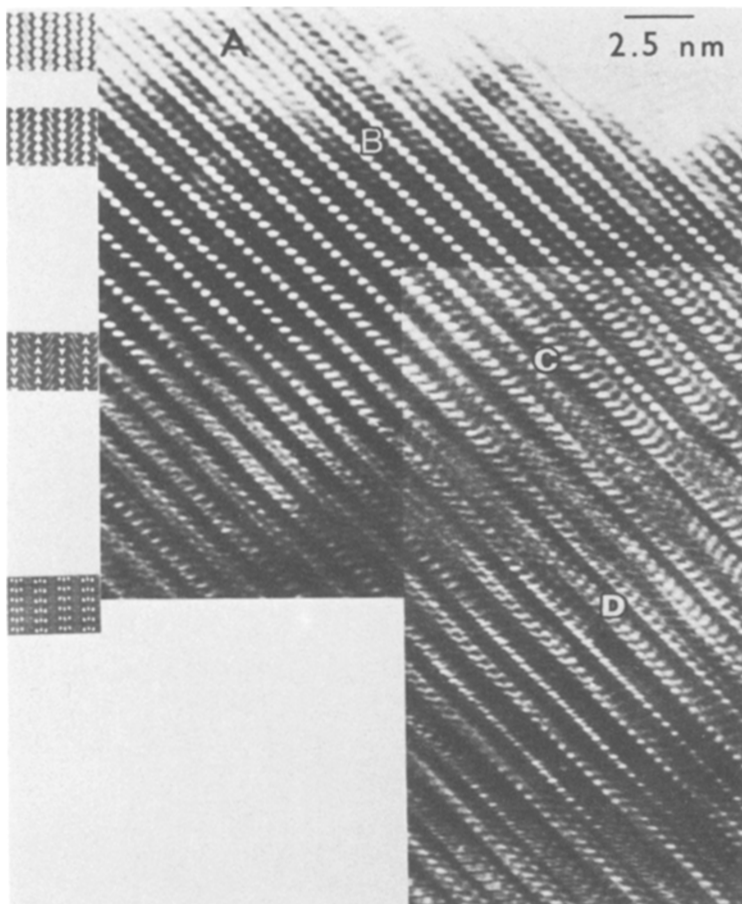

Figure 5 Electron micrograph of a single crystal of sodium beta-alumina along ⟨1 1 $\bar{2}$ 0⟩ matched with computed images at various thickness, using a defocus value of −55 nm. (A) slice 5, ~ 2.8 nm; (B) slice 20, ~11.2 nm; (C) slice 30, ~16.8 nm; (D) slice 50, ~ 27.8 nm.

down any zone, with spots indexed and scaled to the kinematical intensity in the program DIFPAT. The calculated images were produced using the Beevers–Ross coordinates [14] in conjunction with basic crystallographic data [15].

The structure chosen for investigation was a ceramic, sodium beta-alumina, which is a complex spinel of stoichiometric formula $Na_2O \cdot 11Al_2O_3$. It belongs to the space group $P6_3$/mmc, and the unit cell comprises two spinel blocks of close-packed aluminium and oxygen ions separated by Al–O–Al columns across a mirror plane, i.e. the spinel blocks are rotated 180° to each other. The mirror plane contains loosely packed sodium ions which may travel along conduction "tunnels" in the ⟨1 1 $\bar{2}$ 0⟩, ⟨1 0 $\bar{1}$ 0⟩ and ⟨2 1 $\bar{3}$ 0⟩ directions. It is these tunnels which are the noticeable crystallographic feature on all micrographs specifically oriented.

Images of sodium beta-alumina have been calculated for the electron beam along a crystal zone axis of the type ⟨1 1 $\bar{2}$ 0⟩ at various pass-band defocuses, using multiples of a single slice thickness, which in this case was chosen to be equal to the shorter cell dimension, 0.5594 nm. The objective aperture size used in the calculations was 3.9 nm^{-1} corresponding to experimental conditions. Fig. 4 shows the effect of crystal thickness on the computed images at pass-band defocus values at this objective aperture size.

Although it is attempted to take experimental micrographs near optimum defocus, the actual defocus is not known accurately owing to specimen vibration, etc., and is therefore a matter of personal judgement. Pass-band defocuses should produce high contrast images. A comparison of calculated and experimental images should identify the defocus actually used. Examples of this are shown in Figs. 5 and 6. Images at Scherzer defocus, and at low slice numbers, show rows of white spots interspersed with darker regions. These represent the conduction tunnels and the spinel blocks respectively. The general trend is for the size of the conduction tunnels to decrease with

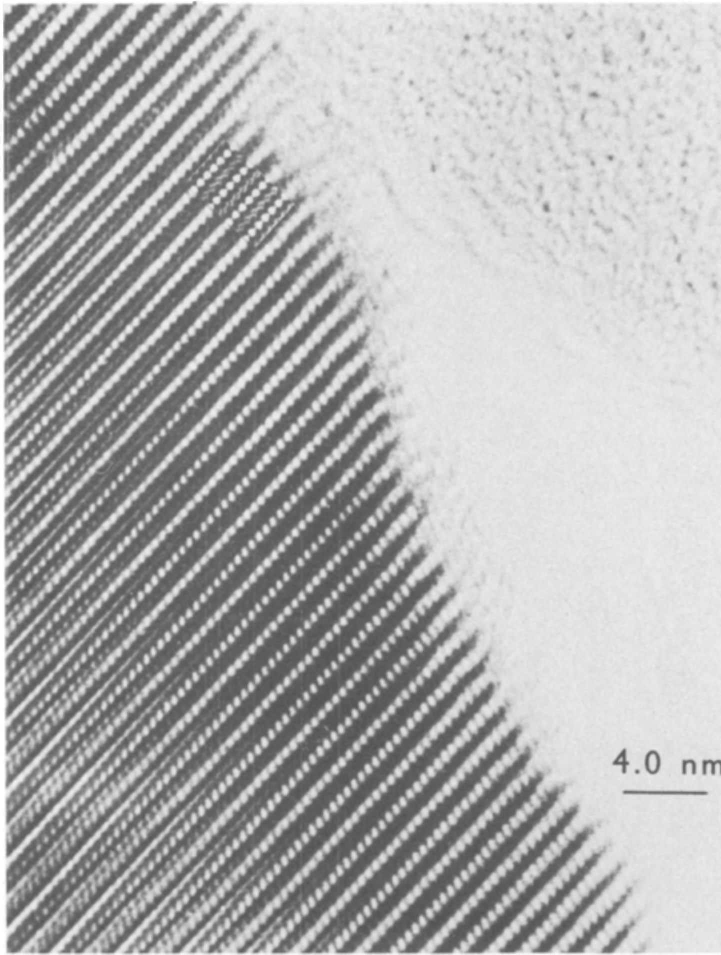

Figure 6 Electron micrograph of a single crystal of sodium beta-alumina along $\langle 11\bar{2}0\rangle$ matched with a computed image corresponding to a thickness of 6.7 nm (slice 12) at a defocus of −55 nm.

increasing thickness, whilst at the same time, there is an increase in the definition of the structure within the spinel blocks.

Pass-band imaging gives rise to greater resolution in the computed images. To obtain the full effect of the pass-band defocus, the size of the objective aperture, R, used in the image, should correspond to the value of the spatial frequency at which the $\sin\chi$ function intersects the u-axis, after the "plateau" in the contrast transfer function (CTF) for that particular defocus has occurred. With reference to the CTFs of Figs. 3c and d, the values of R which should be adopted in image calculations are 4.7 nm^{-1} for the pass-band defocus of −100 nm and 5.0 nm^{-1} for −125 nm. The computed images corresponding to these conditions are shown in Figs. 4i and j and 4k and l. The effect of pass-band imaging may be seen by comparing these images with those of Figs. 4e and f and 4g and h, which are computed at the same defocuses, but use the objective aperture radius of 3.9 nm^{-1}. The change in aperture size for pass-band imaging involves a change in the number of beams contributing to the image.

In order to match experimental and calculated HREM images correctly, it is important to know the crystal thickness. In the present work, there were no crystal defects running from the top to the bottom of the specimen in well-defined directions, the projected lengths of which can be used to estimate a crystal thickness. The thickness was therefore estimated from a comparison of the experimental selected area diffraction pattern with calculated diffracted intensities as described below.

Curves of intensity against crystal thickness are plotted for different beams. The relative intensities of spots in experimental diffraction patterns are compared with the calculated intensities. To a good approximation, the best match gives the average crystal thickness in the experimental

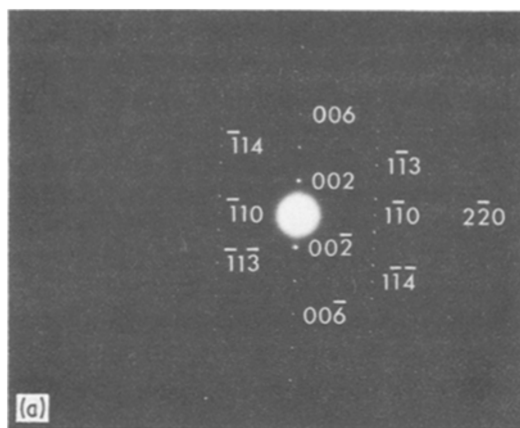

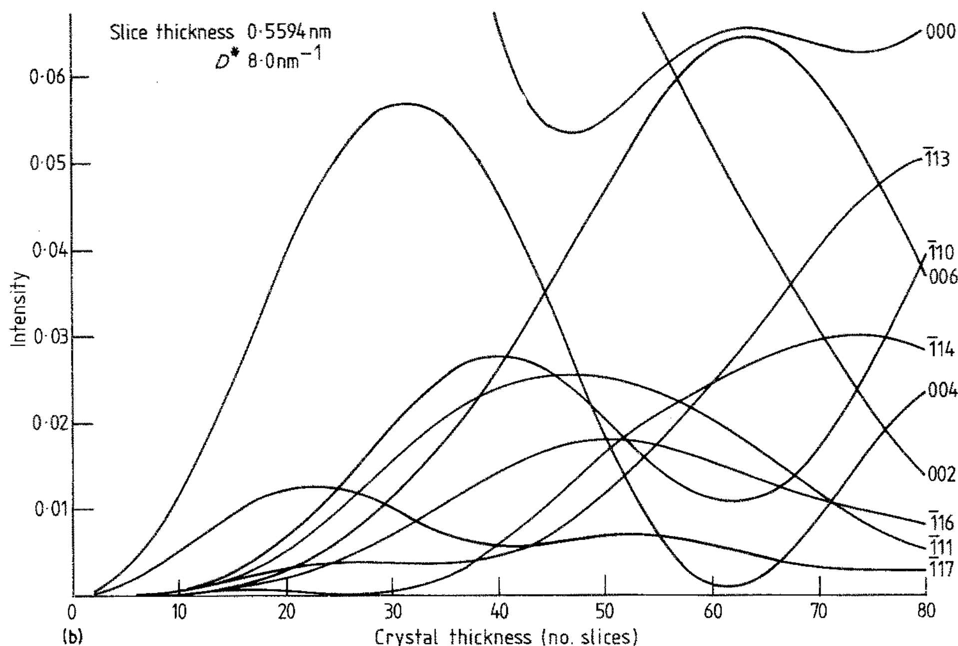

Figure 7 (a) The $\langle 11\bar{2}0\rangle$ diffraction pattern of the crystal shown in Fig. 5. (b) The multi-slice output for reflections along the zone axis $\langle 11\bar{2}0\rangle$ using a slice thickness of 0.5594 nm and reciprocal lattice parameter 8.0 nm^{-1}.

micrograph. An example for which the thickness calculations were carried out is shown in Fig. 7, and the average thickness for the whole crystal was found to be ~ 35 nm.

6. Comment

It is well understood that the resolution of an electron image can be enhanced by adopting the method of recording micrographs at a series of "pass-band" defocuses and recombining these images, taking into account the CTF of the microscope. The difficulty encountered here is the lack of knowledge of the true defocus value in the electron microscope at high magnification. It is hoped that image processing will overcome this problem for both periodic and non-periodic objects, when used as an on-line system attached to the electron microscope. A certain type of image processing [16, 17] can be used as an extension of the structure analysis described above, however it only applies to periodic objects. This system improves the signal-to-noise ratio of an image so that features previously "buried" in the noise become detectable.

Acknowledgement

Many thanks go to Dr C. J. Humphreys of the Department of Metallurgy and Science of Materials at Oxford, who, as my supervisor, gave invaluable held and advice in the study of electron optics and sodium beta-alumina.

References

1. J. M. COWLEY, "Diffraction Physics" (North Holland/American Elsevier, Amsterdam 1975).
2. C. J. HUMPHREYS and J. C. H. SPENCE, *Optik* **58** (No. 2) (1981) 125.
3. M. A. O'KEEFE, 37th Annual Proceedings of the Electron Microscopy Society of America, San Antonio, Texas, August 1979, edited by G. W. Bailey (Claitor's Publicating Division, Baton Rouge, 1979) p. 556.
4. J. M. COWLEY, *Chem. Scripta* **14** (1978–79) 279.
5. J. G. ALLPRESS, E. A. HEWAT, A. F. MOODIE and J. V. SANDERS, *Acta Crystallogr.* **A28** (1972) 528.
6. D. F. LYNCH and M. A. O'KEEFE, *ibid.* **A28** (1972) 536.
7. G. R. ANSTIS, D. F. LYNCH, A. F. MOODIE and M. A. O'KEEFE, *ibid.* **A29** (1973) 138.
8. M. A. O'KEEFE, *ibid.* **A29** (1973) 389.
9. D. F. LYNCH, A. F. MOODIE and M. A. O'KEEFE, *ibid.* **A31** (1975) 300.
10. M. A. O'KEEFE and J. V. SANDERS, *ibid.* **A31** (1975) 307.
11. J. M. COWLEY and A. F. MOODIE, *Proc. Soc. Phys.* **76** (1960) 378.
12. P. GOODMAN and A. F. MOODIE, *Acta Crystallogr.* **A30** (1974) 280.
13. A. J. SKARNULIS, *J. Appl. Crystallogr.* **12** (1979) 636.
14. C. A. BEEVERS and M. A. S. ROSS, *Z. Krist.* **97** (1937) 59.
15. "International Tables for X-ray Crystallography", Vol. 1, edited by N. F. M. Hewry and K. Lonsdale (Kynoch Press, Birmingham, 1965) p. 304 (published for the Union of Crystallography).
16. O. KÜBLER, M. HAHN and J. SEREDYNSKI, *Optik* **51** (1978) 171.
17. *Idem, ibid.* **51** (1978) 235.
18. W. O. SAXTON, "Computing Techniques for Images Processing", Advances in Electronics and Electron Physics, Supplement 10 (Academic Press, London, 1978).

Received 24 June 1982
and accepted 16 June 1983